Journal of
# Materials Chemistry A

# Mechanistic Investigation of Redox Processes in Zn-MnO2 battery in Mild Aqueous Electrolytes

SCHOLARONE™
Manuscripts

# ARTICLE

## Mechanistic Investigation of Redox Processes in Zn-MnO$_2$ battery in Mild Aqueous Electrolytes

‡*Ismael A. Rodríguez-Pérez\**, ‡*Hee Jung Chang\**, ‡*Matthew Fayette\**, *Bhuvaneswari M. Sivakumar, Daiwon Choi, Xiaolin Li, David Reed*

Zinc-MnO$_2$ based batteries have acquired attention for grid-level applications, due to impressive theoretical performance, cost effectiveness and intrinsic safety. However, there are still many challenges that remain elusive due to the complex and controversial mechanisms of operation that hinders commercialization. In this work, the detailed redox processes that occur at the cathode during Zn-MnO$_2$ battery operation are elucidated. Using a blend of structural and electrochemical techniques, the redox pairs that occur during operation are mechanistically studied while also showcasing the true impact of the electrolyte additive (0.1 M MnSO$_4$) in a 1 M ZnSO$_4$ electrolyte. An electrochemical quartz-crystal microbalance (EQCM) has been leveraged to reveal the effect of zinc hydroxy sulfate salt (Zn$_4$SO$_4$(OH)$_6$·nH$_2$O) and zinc manganese oxide (Zn$_x$Mn$_y$O$_z$) dissolution/deposition, which are believed to be major components during discharge and charge conditions. . These results provide insight not currently available, allowing a holistic view of the electrochemical reaction mechanisms during battery operation

## Introduction

Due to the intermittency of renewable energy and the geographical restrictions on several large-scale energy storage solutions such as pumped hydro, electrochemical energy storage remains the enabler for a more sustainable future.[1] Although lithium-ion batteries (LIBs) are currently dominating the market, it is crucial that we find alternative technologies to supplement/compliment them, particularly in large-scale energy storage application. Zinc-based batteries provide some of the most well-known advantages in energy storage today – from high energy and low cost, to exceptional stability and outstanding safety[2–6] with room for improvement. These advantages are paramount in

the competitiveness of the technology, even in the transportation market; zinc-based batteries have the best potential to dominate the large-scale energy storage sector where the levelized cost is imperative and safety is of utmost importance. The concept of an aqueous Zn batteries (AZBs) is not new, but only the alkaline Zn-MnO$_2$ battery has been commercialized as a primary battery due to the lack of a highly reversible electrochemistry. In the last few decades, however, AZBs have made a tremendous comeback in the

field where many groups are now investigating the reversibility challenge for future grid applications due to their unique advantages (i.e. high theoretical capacity (~820 mAh g$^{-1}$) and relatively low standard reduction potential (-0.76 V vs SHE)).[7–10] The three major components of AZBs do not differ from those of LIBs, where the electrolyte and electrodes (anode and cathode) are crucial in their development. The redox mechanism on the anode side is relatively simple in mild aqueous zinc batteries; it is simply electrodeposition and dissolution of the zinc ion onto the zinc metal. Certainly, there are challenges that come with this, but these are beyond the scope of this paper and have been the subject of examination in our previous work.[11] Similarly, the electrolyte is important in the way the AZBs function, from alkaline electrolytes to mildly acidic electrolyte. Both alkaline and mild acidic conditions play different roles and provide different challenges. For example, various cathodes with a variety of structures are under rigorous investigation in the mild acidic electrolyte such as vanadates, phosphates, Prussian blue analogues, hexacyanoferrates, organic materials, and metal oxide cathodes.[12–25] These electrode materials must have redox potentials within the electrochemical stability window of water, as it serves as the electrolyte solvent. Most importantly, they must be amenable towards the storage of cations, but more specifically the charge dense Zn$^{2+}$ ions; a significantly complicated process due to the high charge density of the inserted ions that may warrant structural distortion.[6] Manganese dioxide cathodes are being studied in great depth in mild aqueous electrolytes because of their low cost and high abundance. Among these are various manganese dioxides with different crystallographic structures such as α (1×1), β (2×2), δ (1×1), ε, γ (1×2), λ (1×3) - MnO$_2$.[26] Electrolytic manganese

Energy & Environment Directorate, Pacific Northwest National Laboratory Richland, WA 99352, USA

† Correspondence to: (I.A.R.P.) ismael.rodriguezperez@pnnl.gov;
(H.J.C.) heejung.chang@pnnl.gov;
(M.F.) matthew.fayette@pnnl.gov.

dioxide (EMD or $\varepsilon/\gamma$-$MnO_2$) is widely used for commercial Zn primary batteries due to low production cost, environmental compatibility, high redox potential, and long storage life.[27] As a matter of fact, mechanistic studies of Zn-EMD systems in alkaline systems have been intensively demonstrated.[28] On the contrary, the energy storage process of Zn-EMD in mildly acidic systems is very complex and there is controversy over the storage mechanism; electrochemical redox mechanisms proposed for EMD cathodes span from $Zn^{2+}$ intercalation, to $Zn^{2+}/H^+$ two step co-insertion, and conversion reactions.[9,10,16,29] Recently, work by Li and Chen et al. revealed a functioning mechanism for a $\beta$-$MnO_2$ cathode which suggested a reversible proton insertion, reasons for capacity decay that included the formation of a $Zn_4SO_4(OH)_6 \cdot nH_2O$ (ZHS) layer, and higher performance due to the $Mn^{2+}$ additive in the electrolyte.[30] However, it remains elusive in exactly how much the electrolyte additive contributes towards performance, how much ZHS salt precipitation occurs versus the insertion of $Zn^{2+}/H^+$ ions at the cathode material, and if the ZHS salt precipitation and dissolution is contributing towards the performance of the cathode.

In this work, using advanced structural and electrochemical characterization techniques such as electrochemical quartz-crystal microbalance (EQCM), we have elucidated and proposed an overall mechanistic view of the redox process leading to the energy storage of EMD in a Zn-$MnO_2$ battery with mild acidic aqueous electrolytes. EQCM allows for investigation of redox reactions occurring at the electrode surface and to our knowledge has not been used to investigate EMD electrodes. This, in concert with more conventional techniques such as scanning electron microscopy (SEM), x-ray diffraction (XRD), x-ray photoelectron spectroscopy (XPS), cyclic voltammetry (CV), galvanostatic charge/discharge (GCD) and inductively coupled plasma (ICP) spectrometry, we aim to provide further insights into the storage mechanism of the EMD cathode starting from the significantly different first cycle and its influence on the following cycles.

## Experimental

### EQCM study

Electrochemical QCM (EQCM) measurements were performed with a model QCM 200 (SRS Instruments) The experiments were conducted in a two-electrode cell configuration with the electrodeposited $MnO_2$ on Au as the working electrode and Zn acting as a counter/reference electrode. Quartz Crystal Microbalance (QCM) Au crystal was used as working electrode. The gold working electrode, A = 1.37 $cm^2$, has a resonant frequency of $f_0$ = 5.000 MHz, density of Quartz $\rho$ = 2.648 g $cm^{-3}$, and shear modulus of $\mu$ = 2.947 x $10^{11}$ g $cm^{-1}$ $s^{-2}$. The electrode was cleaned in 1:1 Nitric Acid: Water followed by thorough rinsing with Millipore water (>18.2 M$\Omega$ cm), drying with Argon, and then immersed in the electrochemical cell. Electrodeposited $MnO_2$ films were prepared from a solution of 1 M $ZnSO_4$ (99%, Sigma Aldrich) + 0.1M $MnSO_4$ (99%, Sigma Aldrich). All films were potentiostatically deposited at a potential of 2 V vs. $Zn/Zn^{2+}$, with the target charge being 20 mC (0.0166 mAh). Analysis of the Sauerbrey equation (**eq 1**) indicates that a 1 Hz frequency change corresponds to a mass change of 0.018 $\mu$g $cm^{-2}$.

$$\Delta f = \frac{-2f_0{}^2}{A\sqrt{\mu\rho}}\Delta m$$

(1)

### Electrode and battery preparation

Commercial $MnO_2$ (electrolytic manganese dioxide, EMD) powder from U.S. research group was used as an active material for cathode electrodes. Cathode powders consisted of EMD (70 wt %), acetylene black (20 wt %) and PVdF binders (10 wt %) were mixed to form a slurry using a planetary centrifugal mixer (Thinky mixer, ARE-310) at 2000 rpm for 25 mins and 5 mins for deforming. The slurry then was spread onto a titanium current collector and vacuum-dried overnight at 80°C. For the battery preparation, the cathode electrode was punched into a 0.5-inch diameter disk and the average mass loading was ~1 mg $cm^{-2}$. The zinc anode also was punched into a 0.56-inch diameter disk and glass fiber (Whatman, GF/B) was used as the separator. All cell components were then assembled in CR 2032 coin-type cells.

### Electrochemical Characterization

Cyclic voltammetry (CV) of the EMD electrode was performed from 0 to 0.8 V vs Ag/AgCl (1.0 to 1.8 V vs $Zn^{+2}/Zn$) at 0.001 V $s^{-1}$ in three- electrode configuration with a high surface area activated carbon (AC) counter electrode, and a Ag/AgCl reference electrode. For galvanostatic charge/discharge (GCD) experiments, all the cells were cycled at 100 mA $g^{-1}$ in the voltage window from 0 to 0.8 V vs Ag/AgCl. To investigate the mechanistic insights of the cathodes influenced by electrolytes, control CV and GCD experiments were carried out using an acetylene black (AB) electrode as a cathode. Two different control electrolytes of 1 M $ZnSO_4$ and 1 M $MnSO_4$ were tested, and electrochemical performances of the electrolytes were then compared to the conventional 1 M $ZnSO_4$ + 0.1 M $MnSO_4$ electrolyte. All electrochemical measurements were made using a Biologic VMP3 (Biologic USA) using EC-Lab Software (v. 11.3).

### pH measurements

The pH of electrolyte was measured from the EMD cells in Swagelok type cell using an Orion Star A211 pH Benchtop Meter (Thermo Scientific). For ex-situ pH measurements, the electrolytes after discharge/charge were collected from the EMD cell and the pH probe was vertically immersed in the electrolyte. For in-situ pH measurements, the galvanostatic intermittent titration technique (GITT) was applied to the cell at the current density of 0.03 A/g (C/10) and followed by a 40 min relaxation period. To measure a local pH as accurately as possible, we modified the distance between the anode and cathode by overlapping several layers of separators to place the pH probe in between the electrodes. Finally, the pH values were recorded during relaxation times.

### Inductively Coupled Plasma Spectroscopy

The electrolyte solutions were analyzed using inductively coupled plasma/atomic emission spectrometry (ICP/AES, Optima 7300DV, Perkin Elmer) techniques. The measurements were performed after appropriate dilutions (samples were diluted in order to be able run in the ICP). As a crosscheck for spectral interference, three emission lines were chosen for each element. The calibration standards were matrix-matched in water. To dissolve the solid samples, concentrated hydrochloric acid (HCl 37%, Acros Organics) was used, they were then diluted with deionized water.

*Material Characterization*

The crystal structural phase evolution during electrochemically discharged and charged state of EMD electrodes were characterized by using both an X-ray diffractometer (XRD, Empyrean, Malvern Panalytical Inc., Westborough, MA) with a CuKα sealed tube (λ = 1.54178 Å) and X-ray photoelectron spectroscopy (XPS, Kratos Axis Ultra DLD spectrometer equipped with a high-performance $Al_{K\alpha}$ monochromatic X-ray source (1486.6 eV)). The EMD electrode was collected at the charged and discharged state after two cycles in 1 M $ZnSO_4$ + 0.1 M $MnSO_4$ electrolyte and subjected to both XRD and XPS. The high-resolution spectra were recorded at a pass energy of 20 eV with a step size of 0.1 eV over the analysis area of 700×300 $\mu m^2$. Monoatomic Ar ions at 5 keV were used with a sputter area of about 3mm x 3mm for depth profile analysis. The charge neutralizer with low-energy electrons was used to exclude the surface charging effects, and the binding energy of C 1s at 284.8 eV was used as the charge reference. XPS data were analyzed by Casa XPS software using Gaussian/Lorentzian (GL30) line shape and Shirley background correction. All XPS binding energies reported here are with an uncertainty of ±0.1 eV. The surface of EMD cathode materials was characterized by scanning electron microscopy (SEM, JEOL JSM-7001F field-emission). An Oxford energy-dispersive-x-ray spectroscopy (EDS) with silicon drift detector was conducted for element mapping analysis. For SEM experiments, cathodes retrieved were washed in deionized water and dried at 80°C under vacuum overnight for SEM study.

**Results and discussion**

*Electrochemical exploration of the EMD storage mechanism*

Before investigating the details of electrochemical redox reactions of EMD in mildly acidic electrolytes, cyclic voltammetry (CV) was performed at different scan rates to determine whether the electrochemical reaction kinetics are diffusion or non-diffusion controlled (**Figure S1**). These measurements offer real-time reaction information of the faradaic contribution from the charge-transfer process with surface elements, referred to as capacitive reactions (non-faradaic contribution) from the double layer effect, or faradaic reactions, referred to as diffusion-controlled reactions. Using the power law equation $i=av^b$, where $i$ is the current, $v$ is the scan rate, and $a$ is a coefficient, both anodic and cathodic $b$ values were obtained below 0.5, which implies that the most dominant reactions of EMD in 1 M $ZnSO_4$ electrolyte are diffusion-controlled. **Figure 1** illustrates the CV curves of the EMD cathode and AB cathode in different electrolytes tested at a single scan rate of 0.1 mV/s: 1 M $ZnSO_4$, 1 M $MnSO_4$, and 1 M $ZnSO_4$ + 0.1 M $MnSO_4$. It is important to note that all electrolytes had similar pH values differing by no more than 0.2. A three-electrode cell set-up was employed to differentiate the electrodes (working electrode and
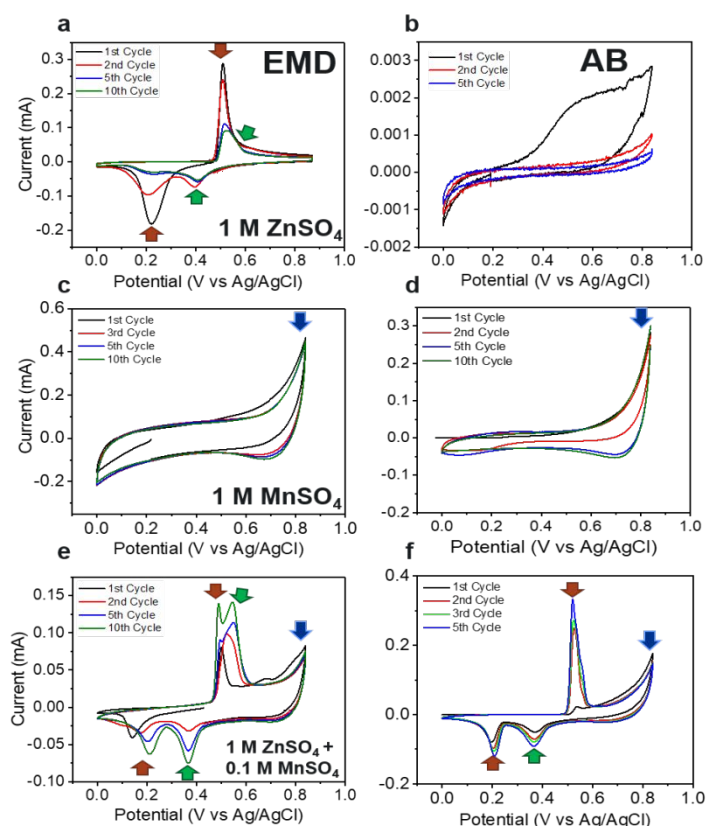


counter electrode) and to monitor them individually by adding the reference electrode (Ag/AgCl) in the mildly acidic electrolyte system. AC was chosen as the counter electrode to eliminate chemistry pertaining to the Zn anode and enable the study of the EMD cathode entirely on its own. Moreover, acetylene black (AB) electrode was used as a control cathode to understand the role of electrolytes by reducing variables as much as possible.

**Figure 1**. (a) CV of EMD in 1 M $ZnSO_4$ (B) CV of AB in 1 M $ZnSO_4$. (c) CV of EMD in 1 M $MnSO_4$ (d) CV of AB in 1 M $MnSO_4$. (e) CV of EMD in 1 M $ZnSO_4$ + 0.1 M $MnSO_4$ (f) CV of AB in 1 M $ZnSO_4$+ 0.1 M $MnSO_4$. Scan Rate= 0.001 V s-1

It is clearly seen in the CV of the EMD cathode with a 1 M $ZnSO_4$ electrolyte that two noticeable redox peaks were observed during reduction at ~0.4 V (vs Ag/AgCl; all V values will be vs Ag/AgCl unless otherwise specified) (green arrow) and ~0.2 V (red arrow) with the corresponding oxidation peaks at ~0.5 V (red arrow) and ~0.57 V (green arrow), except for the 1st cycle (**Figure 1a**). Even though redox peaks are clearly noticeable at the beginning, the performance slowly fades as the 10th cycle is reached. This can be attributed to the Mn dissolution from the cathode into the electrolyte, as can be seen from ICP analysis (**Table S1**); the sample that had been soaked in electrolyte had a lower concentration of Mn, indicating the clear dissolution of Mn into the electrolyte. Furthermore, no redox peaks are observed for the AB cathode with a 1 M $ZnSO_4$ (**Figure 1b**).

It is well known in the literature[16] that the $Mn^{2+}$ additive aids the performance of the system via Le Chatelier's principle, where the concentration of $Mn^{2+}$ in the electrolyte prevents the mass dissolution of the EMD electrode. Therefore, a lower amount of dissolution takes place since equilibrium (rate of dissolution=rate of deposition) is reached sooner. Subsequently, to better understand the effect of the $MnSO_4$ salt additive, the CV experiments were repeated using the EMD and AB cathode with a 1 M $MnSO_4$
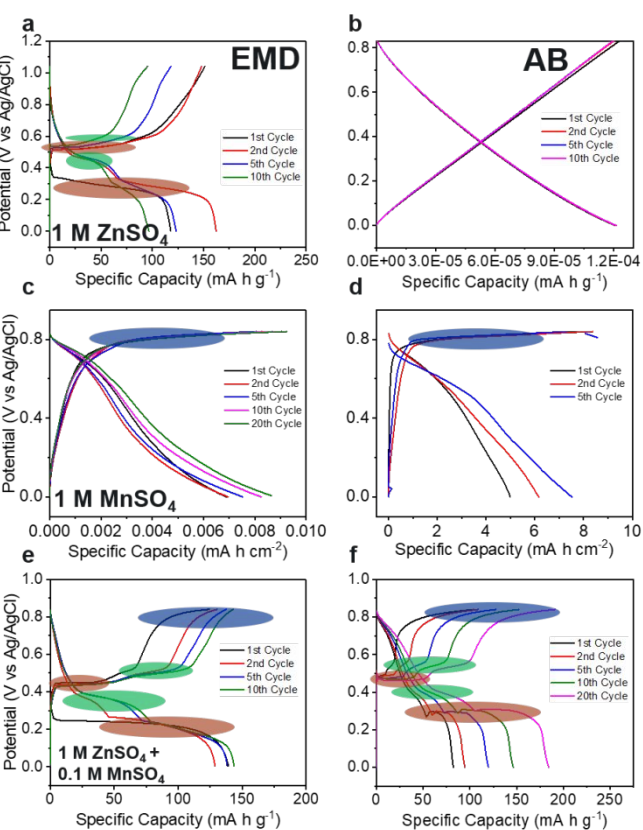
electrolyte (**Figure 1c, d**, respectively). Surprisingly, no redox peaks were observed, for both EMD and AB electrodes where the CV only showed one peak (blue arrow). According to the Mn Pourbaix diagram[31–33], it indicates that $Mn^{2+}$ deposition would begin at ~0.5 V given the pH of the system is ~4.5. Since there is no Zn source in the electrolyte, there is no induced structural change (conversion) of the deposited $MnO_2$, which is identified as an "activation". Without this activation process, the deposited $MnO_2$ is not redox active. Furthermore, without Zn in the electrolyte, $Zn_4SO_4(OH)_6 \cdot nH_2O$ (ZHS) salt deposition has not occurred. Therefore, it became evident that the Zn in the electrolyte was also playing a critical role in promoting redox activity for the EMD cathode. After the control electrolyte experiments, the conventional electrolyte of 1 M $ZnSO_4$ + 0.1 M $MnSO_4$ was tested for both the EMD and the AB cathodes in a CV experiment (**Figure 1e, f**, respectively). The EMD shows two distinguishable redox peaks seen in the CV of EMD with 1 M $ZnSO_4$ (**Figure 1a**). Unlike the CV of 1 M $ZnSO_4$, though, development of the additional peak at ~0.8V (blue arrow) is observed, which indicates significant $MnO_2$ deposition during oxidation. Also, the first cycle is clearly different from the rest with only one cathodic peak at 0.18 V and one anodic



peak at 0.5 V as indicated with red arrows. However, the performance of the AB cathode was not at all expected, the CV is nearly identical to a pure EMD cathode except the first cycle with two cathodic peaks at 0.2 V (red arrow) and 0.38 V (green arrow). Despite the absence of EMD in the beginning, $Mn^{2+}$ additive plays an essential role in generating an in-situ manganese oxide structure during CV with $Zn^{2+}$ in the electrolyte.

**Figure 2**. (a) Charge/discharge curves for EMD/Carbon Fiber Cell in 1 M $ZnSO_4$ (B) Charge/discharge curves for AB/Carbon Fiber Cell in 1 M $ZnSO_4$. (c) Charge/discharge curves for EMD/Carbon Fiber Cell in

1 M $MnSO_4$ (d) Charge/discharge curves for AB/Carbon Fiber Cell in 1 M $MnSO_4$. i= (e) Charge/discharge curves for EMD/Carbon Fiber Cell in 1 M $ZnSO_4$ + 0.1 M $MnSO_4$ (f) Charge/discharge curves for AB/Carbon Fiber Cell in 1 M $ZnSO_4$+ 0.1M $MnSO_4$. 100 mA/g

It is plausible that this in situ EMD deposition on the AB electrode also involved the zinc, activating the as-made EMD structure for further redox activity, hence we see the same CV profile as if it were a pristine EMD cathode. Experimentally, since the open circuit voltage of the AB cell was initially negative, the CV scan initiated anodically, which triggers in situ $Mn^{2+}$ deposition and activation of the electrodeposited (zinc) manganese oxide complex formed from the electrolyte with additive. Therefore, the first cycle of the CV for the AB cell shows both cathodic peaks (0.2 V and 0.4 V) immediately, that are only observable in the second cycle of the EMD half-cell. In the case of the EMD half-cell, however, two cathodic peaks were observed when oxidation of CV was performed first, indicating the oxidation aids in the activation of the EMD (**Figure S2**). It is not clear yet how much initial deposition of the (zinc) manganese oxide complex can activate the second cathodic peak (~0.4 V) and further quantitative studies are needed for future work. Finally, it is strongly evident that the additive in the electrolyte is contributing more to the redox activity than originally anticipated.

The GCD potential profiles (**Figure 2**) are in good agreement with the CV curves. For the EMD with the 1 M $ZnSO_4$ electrolyte (**Figure 2a**), both the charge/discharge plateaus coincide with the anodic/cathodic peaks seen in the CV data. In the first GCD cycle, the discharge and charge plateau marked with the red ovals are observed at ~0.33 V and ~0.51 V, respectively. They correspond to the first cathodic/anodic peak (red arrow) observed in the CV data (**Figure 1a**). Upon the second cycle, a new discharge plateau (green oval) at ~0.45 V is observed, which is in agreement with a newly occurring cathodic peak (green arrow) in the CV second cycle. Using the 1 M $MnSO_4$ electrolyte, there is no clear reversible redox activity for both EMD and AB electrode (**Figure 2c,d**), except the redox activity at high potentials at ~0.8 V, which could indicate $MnO_2$ deposition. In other words, since $Zn^{2+}$ is not present in the electrolyte, neither the structural change of EMD (activation process) nor the salt precipitation (ZHS) occurred. In the GCD profile of the 1 M $ZnSO_4$ + 0.1 M $MnSO_4$ electrolyte, the charge/discharge voltage profiles are consistent with the CV curves for both the EMD cathode and the AB control cathode (**Figure 2e,f**, respectively). It is important to note the difference in the first cycle from the following cycles, especially in CV, where the first cycle is often overlooked in the literature; the details of changes between $1^{st}$ and the following cycles will discussed in the next sections. The cycling performances of both EMD and AB electrode show that the charge/discharge capacity increases for 20 cycles, which is attributed to the continuous deposition of $Mn^{2+}$ from the electrolyte additive. It is clear evidence that the impressive capacities of the control AB electrode prove the significant contribution of the electrolyte (1 M $ZnSO_4$ + 0.1 M $MnSO_4$). By adding more active material - in situ from the electrolyte with $MnSO_4$ additive - an electrodeposited manganese oxide complex on the AB electrode can indeed participate in redox reactions, resulting in operation like an EMD cell.
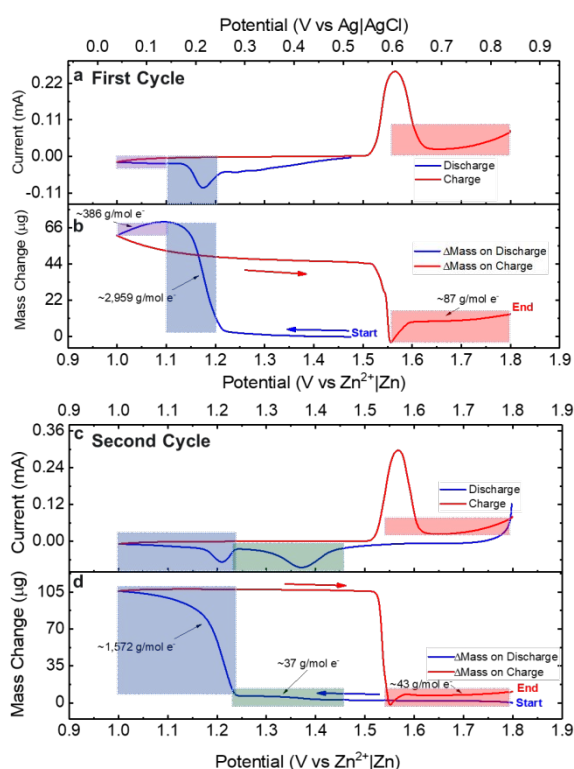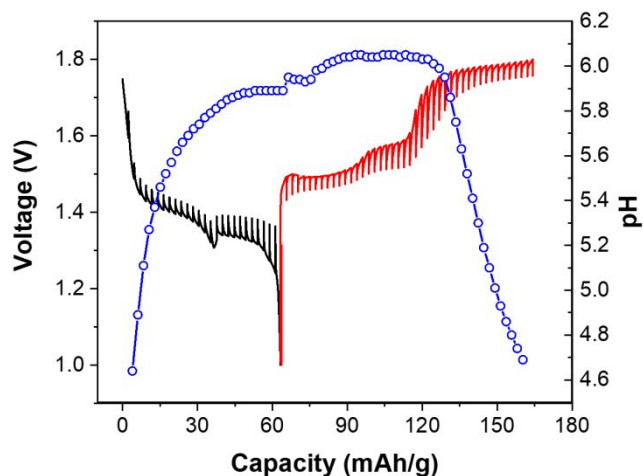
### *In situ EQCM and pH studies on EMD cathode*

The energy storage mechanism of EMD cathode is the subject of much debate as the redox peaks are generally attributed to either $H^+$ and $Zn^{2+}$ insertion separately[34], or jointly.[29] On the other hand, mechanisms focused more on electrochemical deposition/dissolution have been reported recently. However, a clear explanation of the overall charge storage mechanism is still not available due to the complexity of cathode material phases, electrolyte composition, and pH changes during electrochemical cycles. To gain more insight into the overall mechanism of the complex Zn-MnO$_2$ battery system, EQCM measurements were employed coupled with ex-situ pH measurements. It is important to note that the EQCM tests were done with potentials vs Zn/Zn$^{2+}$ and not vs Ag/AgCl. **Figure 3a** shows the CV of an Au QCM electrode after electrochemical deposition of MnO$_2$ (MnO$_2$/Au in 1M ZnSO$_4$ + 0.1M MnSO$_4$ electrolyte). The shape of the CV curve is essentially identical to recent studies of MnO$_2$ in zinc-sulfate electrolyte (including this work).



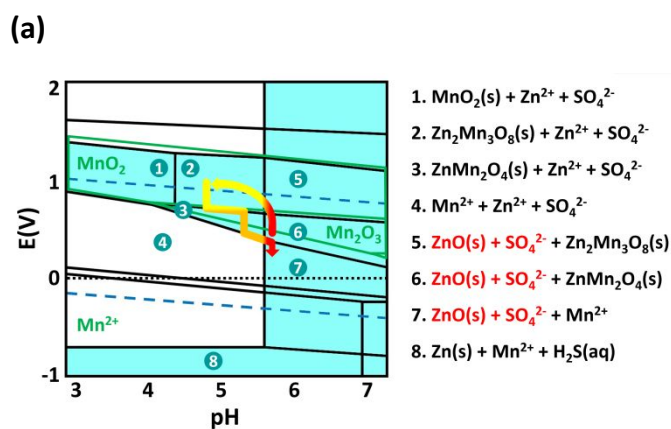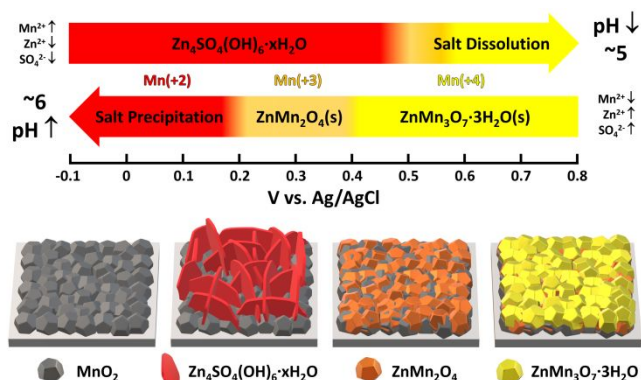**Figure 4**. pH variation of EMD cell during discharge/charge at the current density of 0.03 A g$^{-1}$. Each pH point was recorded during a 40 min relaxation period.

Along with EQCM test, in situ pH measurement was conducted on custom made Swagelok cell to understand the pH change of the aqueous electrolyte during charge/discharge process as shown in **Figure 4**. Initial pH of the 1M ZnSO$_4$ + 0.1M MnSO$_4$ electrolyte was 4.6 but increased to ~6 when fully discharged. Although discharge/charge capacities were relatively lower than that from the coin cell test due to difference in cell setup, the observed pH changes were similar to the previous report. [37]
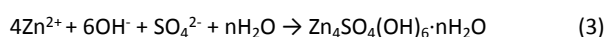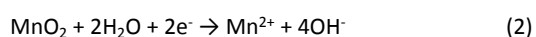


**Figure 3**. (a) 1$^{st}$ cycle CV and (b) EQCM of MnO$_2$/Au electrode 1 M ZnSO$_4$+ 0.1 M MnSO$_4$. (c) 2$^{nd}$ cycle CV and (d) EQCM of MnO$_2$/Au electrode 1 M ZnSO$_4$+ 0.1 M MnSO$_4$. Scan Rate= 0.001 V s$^{-1}$.

**(a)**



1. MnO$_2$(s) + Zn$^{2+}$ + SO$_4^{2-}$
2. Zn$_2$Mn$_3$O$_8$(s) + Zn$^{2+}$ + SO$_4^{2-}$
3. ZnMn$_2$O$_4$(s) + Zn$^{2+}$ + SO$_4^{2-}$
4. Mn$^{2+}$ + Zn$^{2+}$ + SO$_4^{2-}$
5. ZnO(s) + SO$_4^{2-}$ + Zn$_2$Mn$_3$O$_8$(s)
6. ZnO(s) + SO$_4^{2-}$ + ZnMn$_2$O$_4$(s)
7. ZnO(s) + SO$_4^{2-}$ + Mn$^{2+}$
8. Zn(s) + Mn$^{2+}$ + H$_2$S(aq)

**(b)**

**Figure 5**. (a) Pourbaix diagram calculated[31-33] based on 1 M $ZnSO_4$ + 0.1 M $MnSO_4$ electrolyte and **(b)** schematic drawing of EMD cathode phase transitions with potential and pH changes.

For better understanding of the electrochemistry and interpretation of EQCM data, a Pourbaix diagram was generated from the Materials Project[31] as shown in **Figure 5** based on first-principle calculation of phases from Mn, Zn and S elements in 1M $ZnSO_4$ + 0.1M $MnSO_4$ electrolyte concentrations.[32,33] Since the diagram is generated using a density-functional theory (DFT) based material database, any material or phase not yet present in the database is not shown. This lessens the accuracy of the exact phases in the diagram but provides a reasonably accurate trend of valance (or oxidation) states of the elements and phase stability at a given pH, potential, and electrolyte conditions during complex battery operation. As seen in the CV (**Figures 1, and 3**) and GCD data, the first cycle is significantly different from the second cycle, and as such will be addressed separately. During the initial reduction (**Figure 3a,b**), only one cathodic peak with (**Figure 3a**), a mass increase of 66 µg is observed (**Figure 3b**) at ~ 1.2 V vs $Zn^{2+}$/Zn, which agrees with GCD (**Figure 2e**). The mass change associated during the reduction is attributed to the dissolution of $MnO_2$ (**eq 2**), which increases local and/or bulk pH of the electrolyte followed by formation/precipitation of the complex zinc hydroxide sulfate (ZHS: $Zn_4SO_4(OH)_6 \cdot nH_2O$, $0 \leq n \leq 5$) (**eq 3**).[16] The extent of initial $MnO_2$ dissolution depends on the composition, concentration and amount of the electrolyte but then again $MnO_2$ is not a stable phase at the corresponding pH & potential as shown in ❼ of the Pourbaix diagram. Consequently, the $Mn^{2+}$ concentration will increase as concentrations of $Zn^{2+}$ and $SO_4^{2-}$ decrease. The ZHS salt precipitation (**eq 3**) has been previously reported to occur when the pH of the solution reaches 5.4~5.7, which is within the measured pH change between 4.6 and ~6 as shown in **Figure 4**. [37]
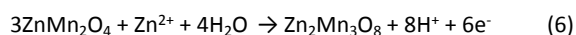
$$MnO_2 + 2H_2O + 2e^- \rightarrow Mn^{2+} + 4OH^- \quad (2)$$

$$4Zn^{2+} + 6OH^- + SO_4^{2-} + nH_2O \rightarrow Zn_4SO_4(OH)_6 \cdot nH_2O \quad (3)$$

From ❼ of the Pourbaix diagram, ZnO + $SO_4^{2-}$ are shown as the stable phase because the ZHS structure is not included in the database but the pH for Zn oxidation/reduction transition is close to the reported pH of 5.56. ZHS precipitates into a layered structure composed of stacked $Zn(OH)_2$ sheets with $ZnSO_4$ and water filling the interlayer spaces. It can be inferred from the mass change that in addition to the ZHS salt precipitation, underlying reactions may occur that activate the EMD for electrochemical storage (i.e. formation of a cathode electrolyte interphase (CEI)- like structure). Interestingly, once below 1.1 V vs $Zn/Zn^{2+}$, there is a mass decrease of 15 µg, which may be certainly due to continuous $Mn^{2+}$

dissolution from the surface $MnO_2$ or $Mn_2O_3$ of EMD as $Zn^{2+}$ is depleted from the electrolyte solution (**Figure 5a**, green line). However, the mass change exceeds the amount expected from only $MnO_2$ dissolution (molecular weight of $MnO_2$ = 86.93 g/mol). This can be rationalized as possible dissolution/delamination of the ZHS salt once pH of the solution has been stabilized, which will be the subject of a future study.

Upon the reverse (anodic) CV scan, the mass equilibrates, meaning no net loss or gain of material is occurring on the electrode surface. At 1.5 V vs $Zn/Zn^{2+}$, the mass decreases by 52 µg which is mostly due to ZHS salt dissolution accompanied by $MnO_2$ or/and $Zn_2Mn_3O_8$ deposition with the possibility of $ZnMn_2O_4$ formation. When fully discharged, the solution is reported to be depleted of $Zn^{2+}$ ion that has been consumed during ZHS formation. Therefore, during initial charge up to 1.5 V vs $Zn/Zn^{2+}$, the electrolyte will contain mostly $Mn^{2+}$ ions, which will be electrochemically deposited as $Mn_2O_3$ followed by conversion to $MnO_2$. The kinetics of manganese oxide deposition are far more sluggish than that of zinc manganese oxide deposition as shown in **Figure 1 c, d** where no distinguishable redox peaks were observed. However, manganese oxide ($Mn_2O_3$ or $MnO_2$) deposition (**eq 4**) decreases the pH below ~5.4 that triggers rapid mass decrease due to ZHS dissolution followed by almost instantaneous mass increase to 6.6 µg attributed to a $MnO_2$ to $ZnMn_2O_4$ conversion and/or $Zn_2Mn_3O_8$ deposition, according to the Pourbaix diagram.

$$Mn^{2+} + 2H_2O \rightarrow MnO_2 + 4H^+ + 4e^- \quad (4)$$
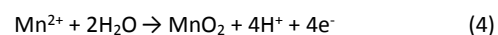
The ZHS salt dissolution is driven by pH decrease during $MnO_2$/$ZnMn_2O_4$ deposition. Such pH decrease can overlap $ZnMn_2O_4$ and $Zn_2Mn_3O_8$ formation according to **eq 5 & 6** as the two-reaction potentials are close to each other at pH lower than 5.5 shown in the Pourbaix diagram ❷ ❸ ❺ ❻ with even the possibility of $MnO_2$ electrodeposition.
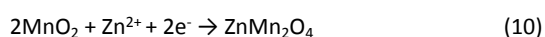
$$Zn^{2+} + 2Mn^{2+} + 4H_2O \rightarrow ZnMn_2O_4 + 8H^+ + 2e^- \quad (5)$$

$$3ZnMn_2O_4 + Zn^{2+} + 4H_2O \rightarrow Zn_2Mn_3O_8 + 8H^+ + 6e^- \quad (6)$$

Additionally, the EMD host material should re-oxidize to $MnO_2$ according to **eq 7**,

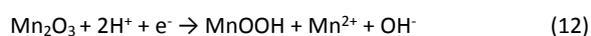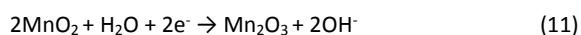$$MnOOH \rightarrow MnO_2 + H^+ + e^- \quad (7)$$
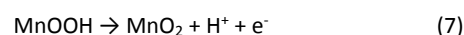
Upon further anodic scanning, the mass increases by ~4 µg by the end of the cycle where more $Zn_2Mn_3O_8$ is deposited. However, it has been reported that $ZnMn_3O_7 \cdot 3H_2O$ is formed at the end of full charge, which is also at $Mn^{4+}$ state.[35,36] Once again, this is possible due to limited phase database used for Pourbaix diagram calculation at room temperature, but the oxidation states of transition metals are quite accurate. If the m/z for the potential range of 1.5~1.8 V vs $Zn/Zn^{2+}$ is considered (~87 g/mol $e^-$), this can be surmised to be a combination of $ZnMn_2O_4$ (1.37 V vs $Zn/Zn^{2+}$), $ZnMn_3O_7 \cdot 3H_2O$ or $Zn_2Mn_3O_8$ (1.52 V vs $Zn/Zn^{2+}$) and/or $MnO_2$ deposition (molecular mass = 86.93 g/mol) coupled with the bulk transition of MnOOH to $MnO_2$. During charging, the rate of ZHS dissolution depends on the local pH change induced by manganese oxide deposition. Although initial electrolyte pH is 4.6, the final charged pH at 1.8 V vs. $Zn/Zn^{2+}$ was ~6, which is close to the reported value of 5.7 with $Mn^{2+}$ depleted and replaced with $Zn^{2+}$ ions in the electrolyte.[37]

Upon commencement of the 2nd cycle, (**Figure 3c,d**), an additional redox peak at ~ 1.4 V vs $Zn/Zn^{2+}$ (**Figure 3c**) (0.4 vs Ag/AgCl)

**ARTICLE**

appeared, which was not observed in the first cycle (**Figure 1a**) since the initial starting cathode material was $MnO_2$ whereas the second cycle starts with $Zn_2Mn_3O_8$ and/or $ZnMn_3O_7 \cdot 3H_2O$. Upon the first reduction, a mass change of 2µg (**Figure 3d**) is observed. This is indicative of the $Zn_2Mn_3O_8$ to $ZnMn_2O_4$ transition according to the simulated Pourbaix diagram ❷ ❸ where $Mn^{4+}$ in $Zn_2Mn_3O_8$ gets reduced to $Mn^{3+}$ in $ZnMn_2O_4$. During this step, Zn is not reversibly inserted into the structure and $Mn^{2+}$ insertion is less likely due to consumption during electrochemical deposition. Therefore, the first reduction has been mostly attributed to insertion of $H^+$ following **eq 8-9** accompanied by significant increase in the electrolyte pH, which could not be rationalized by the mass change observed. Consequently, if $H^+$ co-inserted with $Zn^{2+}$, deposition of ZHS salt is expected as the local pH would increase. Furthermore, the insertion of $Zn^{2+}$ into bulk $MnO_2$ is also possible as shown in **eq 10** below, which aligns with the observed mass increase.

$$Zn_2Mn_3O_8 + 3H^+ + 3e^- \rightarrow Zn_2Mn_3O_5(OH)_3 \qquad (8)$$

$$ZnMn_3O_7 \cdot 3H_2O + 3H^+ + 3e^- \rightarrow ZnMn_3O_4(OH)_3 \cdot 3H_2O \qquad (9)$$

$$2MnO_2 + Zn^{2+} + 2e^- \rightarrow ZnMn_2O_4 \qquad (10)$$

Following this voltage range, a second redox reaction at 1.2 V vs $Zn/Zn^{2+}$ is namely due to the $ZnMn_3O_4(OH)_3 \cdot 3H_2O$, $Zn_2Mn_3O_5(OH)_3$ or $Zn_2MnO_4$ dissolution through $Mn^{3+}$ disproportionation (on the electroactive surface) that results from further $H^+$ insertion. Instantly, this dissolution initiates complex ZHS salt precipitation by increasing the pH above 5.4. It should be noted that the mass change in the $2^{nd}$ cycle (105 µg, **Figure 3d**) is substantially increased and the redox potential is slightly higher than that of the first cycle. This is attributed to the change in cathode composition from pure $MnO_2$ to $Zn_2Mn_3O_5(OH)_3$, $ZnMn_3O_4(OH)_3 \cdot 3H_2O$ or $Zn_2MnO_4$ that increases the amount of $Zn^{2+}$ released from the cathode compared to the first cycle and would result in the formation of a higher amount of the ZHS salt. Additionally, the following processes (**eq 11-13**) may occur, which could generate additional hydroxide ions. During electrochemical oxidation/reduction processes, the pH can fluctuate from 4.6 to 6 but will not come back to initial pH since the cathode composition has changed after the first activation cycle. Our pH measurement shows the pH fluctuation was between 5 ~ 6 in the second cycle which is close to the reported 4.9 to 5.7.[37]

$$2MnO_2 + H_2O + 2e^- \rightarrow Mn_2O_3 + 2OH^- \qquad (11)$$

$$Mn_2O_3 + 2H^+ + e^- \rightarrow MnOOH + Mn^{2+} + OH^- \qquad (12)$$

$$Zn_{0.5}Mn_2O_4 + 3H^+ + 3e^- \rightarrow Zn_{0.5}MnOOH + Mn^{2+} + 2OH^- \qquad (13)$$

*The $OH^-$ for every product would cause a local pH increase, leading to ZHS salt deposition as expressed in **eq 3**.

After the formation of the ZHS salt, the mass on the EQCM surface stabilizes, indicating that no net mass change is observed in contrast to the first cycle. This yields credence to the first cycle activation of the EMD surface that allows for a higher tolerance to dissolution. It should be noted that many groups have used ex-situ techniques (XRD, etc.) to try to elucidate the reduction products for $MnO_2$. This has led to considerable debate as to the structures that exist with $Mn_2O_3$, MnO, and $ZnMn_3O_7$ being considered.[38] These structures have very similar 2-theta values, and due to the nature of XRD (displaying bulk properties) the electroactive surface may not be characterized accurately. Additionally, an electrochemically

deposited phase does not provide high crystallinity, nor long-range order. Due to the precipitation of the ZHS salt, trying to decouple the exact structures on the surface via EQCM cannot be accomplished. As mentioned previously, although the oxidation state is accurate, the exact phase of the EMD cathode at charged/discharged states can be different from the Pourbaix diagram. It can be surmised that a multitude of structures exist, including $ZnMn_3O_7 \cdot 3H_2O$, $Mn_2O_3$, and $ZnMn_2O_4$ that dissolve due to $Mn^{3+}$ disproportionation.[31,39] Based upon the EQCM analysis, upon oxidation (charge), a mass decrease of 105 µg upon completion of the anodic peak was found due to the complex ZHS salt dissolution, which in turn was triggered by pH decrease upon $MnO_2$ deposition/re-oxidation due to proton de-insertion. Additionally, there is a net loss of 4 µg compared to the first cycle in which only 2 µg was lost. Lastly, once again from 1.55 V to 1.8 V vs $Zn/Zn^{2+}$, there is a mass change of 11µg, which can be attributed to continuous $ZnMn_3O_7 \cdot 3H_2O$ and/or $MnO_2$ deposition at those potentials. It is recently reported that the charged product is a mixture of broken tunnel variants of $\alpha$-$MnO_2$, $ZnMn_3O_7 \cdot 3H_2O$ and $ZnMn_2O_4$. In this second cycle, however, the m/z is 43 g/mol $e^-$. Considering that the oxidation of $Mn^{2+}$ is a two-electron process, this corresponds to 86 g/mol, which is the molecular weight of $MnO_2$. It can therefore be deduced that no additional products are forming during charge and we have a stable $ZnMn_3O_7 \cdot 3H_2O$ deposition, which is quasi-reversible on discharge, contributing to the high performance of the system due to increased active material.

Therefore, to clarify the actual phases formed during the electrochemical cycling, EMD powder, pristine EMD cathode, electrochemically fully discharged and charged EMD cathodes were subjected to XRD and XPS characterization as shown in **Figure 6**.
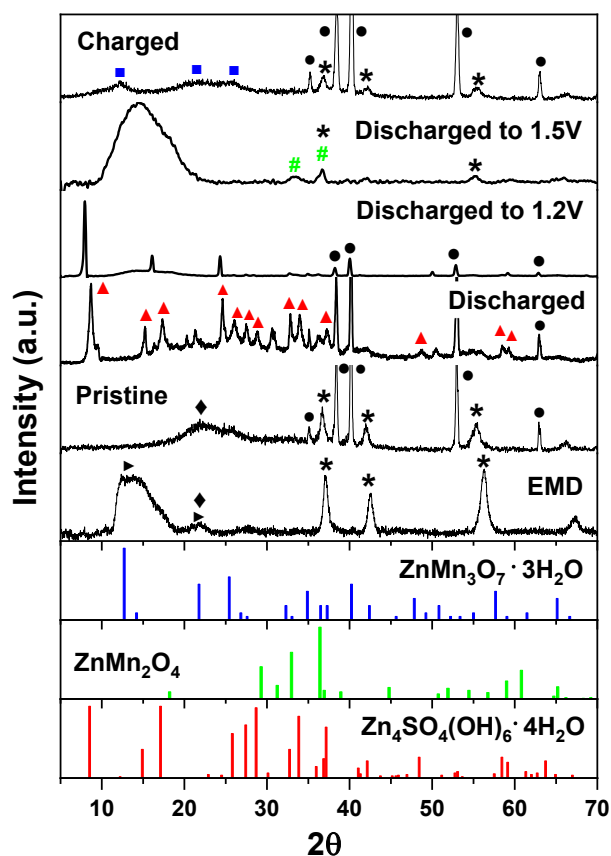
**Figure 6**. XRD patterns of EMD powder, pristine, charged and discharged EMD cathodes. (● Ti mesh, ► Birnessite, ♦ Akhtenskite, * Ramsdellite, ■ $ZnMn_3O_7 \cdot 3H_2O$, # $ZnMn_2O_4$, ▲ $Zn_4SO_4(OH)_6 \cdot 4H_2O$, Ti substrate was removed from the discharge to 1.5V sample for better resolution)

The XRD pattern of commercial EMD was close to ramsdellite (R-$MnO_2$), akhtenskite (ε-$MnO_2$) and birnessite (δ-$MnO_2$ ) mixture in 27:31:42 fractions.[36] The R-$MnO_2$ structure is very close to γ-$MnO_2$ with the most important distinction in patterns being some sets of neighboring reflections which are distinct in the pattern of R-$MnO_2$ and are present as merged, broad single reflections in the case of γ-$MnO_2$.[40] The difference between the phases is the lack of long-range order in γ-$MnO_2$ due to defects. A very intense reflection is at 11.8° which is due to the (001) reflection of birnessite. Once EMD electrode is discharged to 1.5V, tetragonal (I41/amd) $ZnMn_2O_4$ (JCPDS 00-024-1133) seems to appear although XRD peaks are relatively small and amorphous. This is likely due to low temperature electrochemical deposition process confined to the surface of EMD, which cannot be highly crystalline phase. When discharge further to 1.2V, highly crystalline ZHS salt started to form and when fully discharged, intense reflections, attributed to triclinic $Zn_4SO_4(OH)_6 \cdot 4H_2O$ (ZHS, JCPDS 00-044-0673) appeared. Conversely, at a fully charged state, the broad reflection close to rhombohedral (R-3) $ZnMn_3O_7 \cdot 3H_2O$ (JCPDS 00-015-0807) is observed, confirming previous reports.

In order to gain further insight and identify the surface chemistry of the EMD electrode at charged/discharged states exclusively, XPS analyses were conducted on the same samples used for XRD as shown in **Figure 7**.
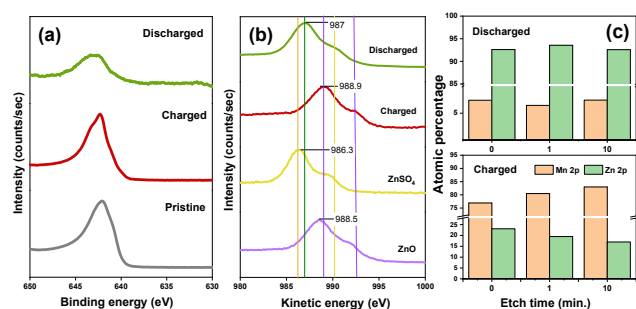


**Figure 7**. XPS spectra of (a) Mn 2P, (b) Zn-LMM for standard ZnO, $ZnSO_4$, pristine and charged/discharged electrode samples and (c) Zn/Mn ratio vs. etched depths of EMD cathode after 2 cycles in 1M $ZnSO_4$ + 0.1M $MnSO_4$.

**Figure 7a** shows Mn 2P XPS spectra for cathode samples under charged and discharged conditions along with a pristine electrode. Two peaks centered around 642 and 645 eV with a spin-energy separation of ~12eV, representing Mn $2p_{3/2}$ and Mn $2p_{1/2}$ components, respectively. The Mn 2p spectra of the charged electrode display the signature photoemission of $Mn^{4+}$ similar to a pristine $MnO_2$ electrode, albeit with noticeable shape change ($MnO_2$ has a much narrower $Mn2p_{3/2}$ peak compared to MnO or $Mn_2O_3$) indicating changes in chemical environment. Conversely, the discharged sample displays significant line broadening (~ eV FWHM) indicating distribution of chemical shift arising from multiple Mn oxidation states, namely $Mn^{2+}$, $Mn^{3+}$ and $Mn^{4+}$. The observed changes on Mn2p spectra upon cycling agree with **eq 7-12**.

To evaluate the chemical environment of Zn, the Zn-LMM Auger lines were probed as they are more sensitive to chemical environments than the traditional Zn 2p spectra. **Figure 7b** shows the Zn LMM for standards ZnO, $ZnSO_4$ and a pristine $MnO_2$ electrode which is represented in Kinetic energy for ease of peak referencing (https://xpssimplified.com/elements/zinc.php). It should be noted that the Zn-LMM Auger lines of both electrodes are different from $ZnSO_4$. This implies the measured Zn-LMM spectra are a direct measure of the active material evolution and absence of surface adsorbed electrolyte materials. For charged electrodes, this peak appears at 988.9 which resembles the ZnO spectra, indicating the O-Zn-O bonding environment. This is in good agreement with the formation of $ZnMn_3O_7 \cdot 3H_2O$ or $Zn_2Mn_3O_8$ during the charging process (*vide supra*). The discharged sample shows ~2 eV shift towards lower energy indicating significant changes in electron density around the Zn atom in the structure.

To further evaluate these structural evaluations across the bulk phase a depth profile analysis was performed for both charged and discharged electrode samples. The atomic percentage of Zn and Mn with respect to etch time is plotted in **Figure 7c.** The Mn 2p and Zn-LMM spectra for both electrodes register a slightly different trend as that of charged and discharged electrodes after 10 minutes of sputtering. For the discharged electrode, Zn was over 90% due to the thick ZHS layer but for the charged electrode the Zn/Mn ratio decreased from 0.3 to 0.2 after 10 min of etching. This corresponds to the $ZnMn_3O_7 \cdot 3H_2O$ (Zn/Mn=0.33) phase but the decrease to 0.2 shows that surface and bulk chemistry is different and most likely formed by electrochemical deposition and possible $Zn^{2+}$ insertion into the bulk $MnO_2$.
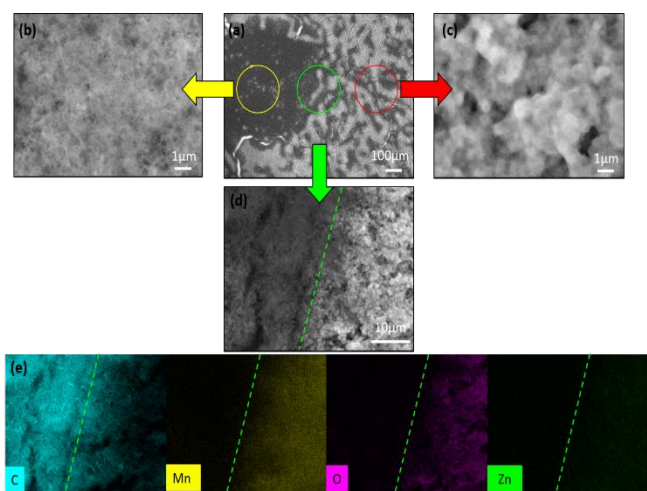
**Figure 8**. SEM images of charged AB electrodes at 100 mA/g after 100 cycles in 1M $ZnSO_4$ + 0.1M $MnSO_4$. (a) AB electrode surface at low magnification. (b) dark area of (a). (c) light area of (a). (d) SEM with boundary between dark and light area. (e) EDX images of (d) showing zinc manganese oxide deposition in the light area.

Finally, to verify redox reactions are mainly based on electrochemical deposition/dissolution of Zn and Mn ions, SEM with EDX mapping analysis were conducted for the AB electrode, which showed the same performance as that of EMD electrode in 1M $ZnSO_4$ + 0.1M $MnSO_4$. **Figure 8a** presents the overall surface morphology of the AB electrode at low magnification (100x) after charging. Two distinguishable areas were observed with different morphological structures as shown in **Figure 8a** and **7d**. In dark areas (**Figure 8b**), very dense and nanoparticulate grains are uniformly and firmly distributed on the surface while round shaped particles of larger size (~1μm in diameter) are detected in the light area (**Figure 8c**). To obtain chemical information, the area where both dark and light segments exist was captured and analyzed (**Figure 8d**). In **Figure 8e**, EDX mapping images confirm that those micro-size particles seen in light area are clearly zinc manganese oxide products formed after the charging process in a 1 M $ZnSO_4$ + 0.1 M $MnSO_4$ electrolyte, whereas the compact nano-size particles which are mostly carbon are observed in dark area. Furthermore, the discharged AB electrode shows flakes with thin and flat sides; EDX can confirm those microstructures are ZHS salt products as shown in **Figure S3**.

## Conclusions

Mechanistic insights for the redox processes that occur during charge and discharge of the EMD cathode have been elucidated.

## Notes and references

[1]    P. C. K. Vesborg, T. F. Jaramillo, *RSC Adv.* **2012**, *2*, 7933.
[2]    X. Ji, H. Jiang, *Chem. Res. Chin. Univ.* **2020**, *36*, 55.
[3]    J. Ming, J. Guo, C. Xia, W. Wang, H. N. Alshareef, *Materials Science and Engineering: R: Reports* **2019**, *135*, 58.
[4]    Y. Li, J. Fu, C. Zhong, T. Wu, Z. Chen, W. Hu, K. Amine, J. Lu, *Advanced Energy Materials* **2019**, *9*, 1970001.
[5]    G. Fang, J. Zhou, A. Pan, S. Liang, *ACS Energy Lett.* **2018**, *3*, 2480.
[6]    W. Xu, Y. Wang, *Nano-Micro Lett.* **2019**, *11*, 90.

Using a combination of structural and electrochemical techniques, including CV, GCD, and most importantly EQCM, the redox pairs occurring during charge/discharge have been analyzed. A control electrode and electrolytes were used to assess the true impact of having the Mn additive, where it was shown that a blank AB electrode had the same level of performance compared to a EMD cathode, showcasing the true impact of the additive in the electrolyte. Structural characterization confirmed that significant formation and deposition of $ZnMn_3O_7.3H_2O$ occurs during charging. On the other hand, ZHS salt deposition is a major phenomenon during discharge in a 1 M $ZnSO_4$ + 0.1 M $MnSO_4$ electrolyte. Most notably, our EQCM results revealed insights not seen in the literature before, revealing that the reduction of EMD consists of an insertion of $Zn^{2+}$ followed by $H^+$ after an electrochemical activation during the initial cycle. Consequently, all CV, EQCM, Pourbaix diagram, XRD and XPS results are in good agreement. It should be mentioned that in an aqueous system, electrode materials' phase and stability are strongly influenced by the pH of the electrolyte. Also, if $H^+$ or $OH^-$ ions are inserted/extracted into/from the electrode, large variations of the pH will occur. Such pH variations will also take place if there is any electrochemical deposition/dissolution process, as in the current mild acidic Zn-$MnO_2$ battery system using the $MnSO_4$ electrolyte additive. Therefore, it is going to be a major challenge when the electrode/electrolyte ratio increases to increase the energy density of the battery.

## Author Contributions

The manuscript was written through contributions of all authors. All authors have given approval to the final version of the manuscript. ‡These authors contributed equally.

## Conflicts of interest

There are no conflicts to declare

## Acknowledgements

[7]    T. Yamamoto, T. Shoji, *Inorganica Chimica Acta* **1986**, *117*, L27.
[8]    C.-C. Yang, S.-J. Lin, *Journal of Power Sources* **2002**, *112*, 174.
[9]    C. Xu, B. Li, H. Du, F. Kang, *Angewandte Chemie International Edition* **2012**, *51*, 933.
[10]   B. Lee, H. R. Lee, H. Kim, K. Y. Chung, B. W. Cho, S. H. Oh, *Chem. Commun.* **2015**, *51*, 9265.
[11]   M. Fayette, H. J. Chang, I. A. Rodríguez-Pérez, X. Li, D. Reed, *ACS Appl. Mater. Interfaces* **2020**, *12*, 42763.
[12]   C. Yuan, Y. Zhang, Y. Pan, X. Liu, G. Wang, D. Cao, *Electrochimica Acta* **2014**, *116*, 404.

[13]    L. Zhang, L. Chen, X. Zhou, Z. Liu, *Scientific Reports* **2015**, *5*, 18263.

[14]    D. Kundu, B. D. Adams, V. Duffort, S. H. Vajargah, L. F. Nazar, *Nature Energy* **2016**, *1*, 16119.

[15]    X. Dai, F. Wan, L. Zhang, H. Cao, Z. Niu, *Energy Storage Materials* **2019**, *17*, 143.

[16]    H. Pan, Y. Shao, P. Yan, Y. Cheng, K. S. Han, Z. Nie, C. Wang, J. Yang, X. Li, P. Bhattacharya, K. T. Mueller, J. Liu, *Nature Energy* **2016**, *1*, 16039.

[17]    Q. Zhao, W. Huang, Z. Luo, L. Liu, Y. Lu, Y. Li, L. Li, J. Hu, H. Ma, J. Chen, *Science Advances* **2018**, *4*, eaao1761.

[18]    X. Wang, F. Wang, L. Wang, M. Li, Y. Wang, B. Chen, Y. Zhu, L. Fu, L. Zha, L. Zhang, Y. Wu, W. Huang, *Advanced Materials* **2016**, *28*, 4904.

[19]    N. Zhang, Y. Dong, M. Jia, X. Bian, Y. Wang, M. Qiu, J. Xu, Y. Liu, L. Jiao, F. Cheng, *ACS Energy Lett.* **2018**, *3*, 1366.

[20]    N. Yesibolati, N. Umirov, A. Koishybay, M. Omarova, I. Kurmanbayeva, Y. Zhang, Y. Zhao, Z. Bakenov, *Electrochimica Acta* **2015**, *152*, 505.

[21]    P. He, G. Zhang, X. Liao, M. Yan, X. Xu, Q. An, J. Liu, L. Mai, *Advanced Energy Materials* **2018**, *8*, 1702463.

[22]    L. Zhang, L. Chen, X. Zhou, Z. Liu, *Advanced Energy Materials* **2015**, *5*, 1400930.

[23]    Z. Guo, Y. Ma, X. Dong, J. Huang, Y. Wang, Y. Xia, *Angewandte Chemie 0*.

[24]    B. Häupler, C. Rössel, A. M. Schwenke, J. Winsberg, D. Schmidt, A. Wild, U. S. Schubert, *NPG Asia Materials* **2016**, *8*, e283.

[25]    F. Wan, L. Zhang, X. Wang, S. Bi, Z. Niu, J. Chen, *Advanced Functional Materials 0*, 1804975.

[26]    W. Wei, X. Cui, W. Chen, D. G. Ivey, *Chem. Soc. Rev.* **2011**, *40*, 1697.

[27]    A. Biswal, B. C. Tripathy, K. Sanjay, T. Subbaiah, M. Minakshi, *RSC Adv.* **2015**, *5*, 58255.

[28]    W. Taucher, K. Kordesch, In *Studies in Environmental Science* (Ed.: Sequeira, C. A. C.), Elsevier, **1994**, pp. 163–202.

[29]    W. Sun, F. Wang, S. Hou, C. Yang, X. Fan, Z. Ma, T. Gao, F. Han, R. Hu, M. Zhu, C. Wang, *J. Am. Chem. Soc.* **2017**.

[30]    L. Li, T. K. A. Hoang, J. Zhi, M. Han, S. Li, P. Chen, *ACS Appl. Mater. Interfaces* **2020**, *12*, 12834.

[31]    A. Jain, S. P. Ong, G. Hautier, W. Chen, W. D. Richards, S. Dacek, S. Cholia, D. Gunter, D. Skinner, G. Ceder, K. A. Persson, *APL Materials* **2013**, *1*, 011002.

[32]    K. A. Persson, B. Waldwick, P. Lazic, G. Ceder, *Phys. Rev. B* **2012**, *85*, 235438.

[33]    A. K. Singh, L. Zhou, A. Shinde, S. K. Suram, J. H. Montoya, D. Winston, J. M. Gregoire, K. A. Persson, *Chem. Mater.* **2017**, *29*, 10159.

[34]    M. Chamoun, W. R. Brant, C.-W. Tai, G. Karlsson, D. Noréus, *Energy Storage Materials* **2018**, *15*, 351.

[35]    D. Wu, L. M. Housel, S. J. Kim, N. Sadique, C. D. Quilty, L. Wu, R. Tappero, S. L. Nicholas, S. Ehrlich, Y. Zhu, A. C. Marschilok, E. S. Takeuchi, D. C. Bock, K. J. Takeuchi, *Energy Environ. Sci.* **2020**, *13*, 4322.

[36]    E. Moazzen, E. V. Timofeeva, C. U. Segre, *J Mater Sci* **2017**, *52*, 8107.

[37]    B. Lee, H. R. Seo, H. R. Lee, C. S. Yoon, J. H. Kim, K. Y. Chung, B. W. Cho, S. H. Oh, *ChemSusChem* **2016**, *9*, 2948.

[38]    Y. Li, S. Wang, J. R. Salvador, J. Wu, B. Liu, W. Yang, J. Yang, W. Zhang, J. Liu, J. Yang, *Chem. Mater.* **2019**, *31*, 2036.

[39]    K. W. Nam, H. Kim, J. H. Choi, J. W. Choi, *Energy Environ. Sci.* **2019**, *12*, 1999.

[40]    E. D. Rus, G. D. Moon, J. Bai, D. A. Steingart, C. K. Erdonmez, *J. Electrochem. Soc.* **2015**, *163*, A356.